(Received 15 October 2025, Accepted 14 November 2025, Scheduled 6 January 2026)

An Innovative Electromagnetic Vector Antenna Design for HF Angle of Arrival

Wei Qiao[1], Chen Zhou[1,*], Mingjie Lv[1], and Qiong Tang[2]

[1]School of Earth and Space Science and Technology, Wuhan University, Wuhan 430072, China
[2]School of Electrical and Information Engineering, Wuhan Institute of Technology, Wuhan 430205, Hubei, China

ABSTRACT: This paper addresses the need for compact, broadband vector-field sensing in high-frequency (HF) direction finding and polarization diverse applications. A compact electromagnetic vector antenna (EMVA) operating over the 3–30 MHz band is proposed, capable of simultaneously sensing all six Cartesian components of the electromagnetic field. The antenna integrates three orthogonal dipoles and three orthogonal loops co-located at a common phase center (CPC), enabling full vector-field reconstruction while avoiding baseline-induced phase errors. A transformer-assisted broadband passive matching network is employed to accommodate the highly reactive impedance of electrically small HF elements, with measured insertion loss and inter-port isolation suitable for practical operation. Field experiments using an 11 MHz ionospheric sounding link validated the effectiveness of the antenna, achieving RMS direction-of-arrival errors of 10.02° (azimuth) and 8.42° (elevation) for O-mode signals and 14.77°/26.09° for X-mode signals. These results demonstrate the suitability of the proposed CPC EMVA for compact polarization-diverse sensing on mobile and space-constrained HF platforms.

1. INTRODUCTION

Polarization, together with frequency, amplitude, and direction, is a fundamental attribute of electromagnetic (EM) waves. Utilizing polarization improves multi-parameter estimation in radar and wireless systems [1–3], enhances communication capacity through 3-D electric-field sensing [4], and mitigates polarization fading in multipath environments [5, 6]. In radar and ionospheric applications, polarization diversity is critical for accurate DOA estimation and O/X-mode separation [7–13].

Electromagnetic vector antennas (EMVAs) measure both electric and magnetic fields and enable full characterization of incoming waves. A full EMVA typically comprises three orthogonal dipoles and three orthogonal loops [14, 15]. Classical six-channel designs, such as SuperCART, demonstrated the feasibility of HF vector sensing but exhibited limited port isolation and was not optimized for DOA estimation [3, 16, 17].

Recent advancements further highlight the relevance of vector sensing at HF. EMVA-MIMO (multiple-input multiple-output) radar has improved 2-D direction of arrival (DoA) estimation and auxiliary localization through tensor modeling and sparse-array formulations [18, 19]. At the antenna level, compact EMVA structures with improved mechanical symmetry and higher isolation have been developed for HF sensing [20], while near-field EMVA-MIMO techniques underline the need for coherent polarization response and aligned phase centers in practical systems [21]. Moreover, recent sensitivity analyses show that co-located dipole-loop triads can outperform traditional dipoles or tripoles in low-frequency environments [22].

Despite these developments, achieving a compact, broadband HF vector antenna with consistently high inter-port isolation remains challenging. Electrically small dimensions and strong ground coupling degrade impedance stability and polarization fidelity, and many existing EMVA configurations still suffer from spatially separated phase centers or insufficient isolation — issues that directly impact DOA and polarization reconstruction performance.

To address these limitations, this work proposes a mechanically symmetric six-port EMVA integrating three orthogonal dipoles and three orthogonal loops at a CPC. The design achieves broadband passive matching and isolation better than −30 dB across 3–30 MHz. Full-wave simulations, prototyping, and ionospheric-sounding experiments validate its performance, yielding RMS DOA errors of 10.02°/8.42° (azimuth/elevation) for O-mode and 14.77°/26.09° for X-mode signals, demonstrating its suitability for HF vector-field sensing and polarization-diverse DOA applications.

2. ANTENNA THEORY AND DESIGN

To facilitate a clear presentation of the multi-polarized antenna architecture, this section provides an overview of the configuration, the dimension-optimization process, and the geometric constraints that ensure a CPC for all six sensing elements. These descriptions establish the basis for the subsequent prototype implementation and performance evaluation.

2.1. Simulation and Analysis of Antenna Configuration

Conventional scalar antennas measure only a single component of the EM field and therefore provide limited informa-

* Corresponding author: Chen Zhou (chenzhou@whu.edu.cn).

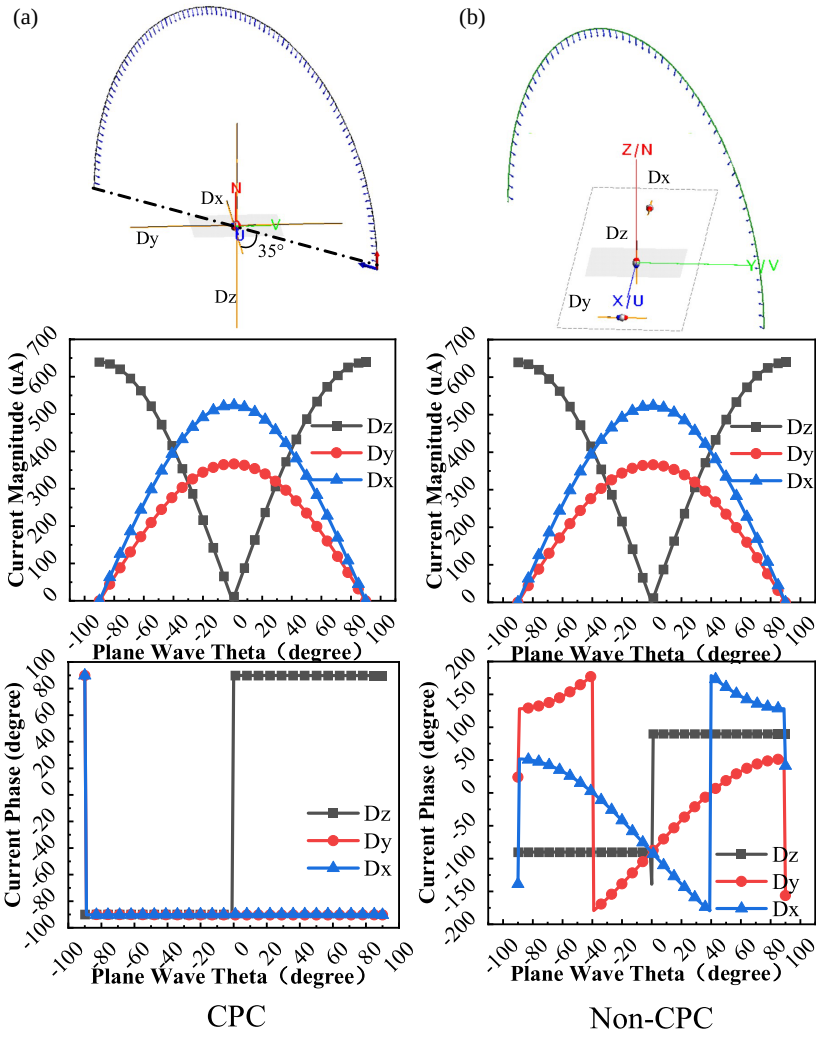

FIGURE 1. Comparison of the electric-field responses of an orthogonal dipole triad under plane-wave excitation for (a) the common-phase-center (CPC) configuration and (b) the non-CPC configuration.

tion for polarization-diverse sensing or angle of arrival (AoA). In contrast, an EMVA can be viewed as a specialized array in which each element is designed to sense a specific component of the incident electromagnetic field. For the electric-field triad, three mutually orthogonal dipoles are employed to measure the three projections of the incident electric field. However, such a dipole triad may be implemented either in a CPC configuration, where all elements share the same spatial origin, or in a non-CPC configuration, where spatial offsets introduce baseline-dependent phase delays.

To verify the distinction between these two configurations, FEKO simulations were conducted under plane-wave excitation. Fig. 1 illustrates the simulated current responses of the orthogonal dipole triad under plane-wave excitation.

The simulation results show the following behavior as the incident plane-wave elevation angle θ varies from $-90°$ to $90°$. At $\theta = \pm 90°$, the incident field is purely vertically polarized, and only the Z-directed dipole (Dz) is excited. As the wave direction changes from $-90°$ to $0°$, the x- and y-components of the electric field gradually increase while the z-component decreases, reaching zero when the incident direction becomes broadside ($\theta = 0°$). Consequently, the current amplitude on Dz becomes minimal at $\theta = 0°$, whereas the currents on Dx and Dy reach their maxima. When θ increases from $0°$ to $90°$, the process reverses, restoring the dominance of the z-component at grazing incidence.

For the dipole current phases, the Z-directed dipole (Dz) exhibits a $180°$ phase reversal as θ crosses $0°$, corresponding to the transition of the incident electric-field projection from negative to positive. In contrast, the phases of Dy and Dz remain essentially unchanged throughout the entire angular sweep because their excitation polarity does not change with θ. These observations are consistent with the physical interpretation of the dipole-field interaction and match the simulated current-phase traces shown in Fig. 1.

For the non-CPC configuration, the three orthogonal dipoles are no longer co-located, and the spatial separation introduces additional geometric phase delays. As the incident plane-wave elevation angle θsweeps from $-90°$ to $90°$, the current amplitudes on Dx, Dy, and Dz still follow the expected field-projection behavior, i.e., Dz dominates at grazing incidence ($\theta = \pm 90°$), while Dx and Dy reach their maxima near broadside ($\theta = 0°$). However, unlike the CPC case, the current phases no longer remain constant with respect to θ. Instead,

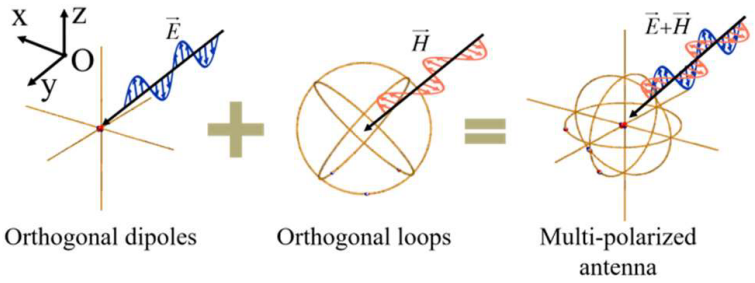

FIGURE 2. Evolution of the EMVA. (The black arrow represents a wave vector, the orange arrow represents the corresponding magnetic field vector, and the blue arrow represents the corresponding electric field vector.).

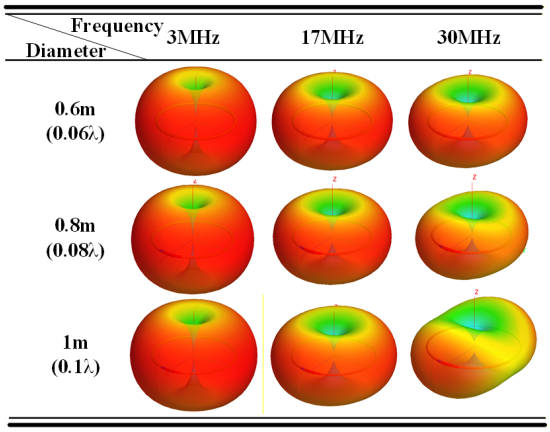

FIGURE 3. Normalized radiation patterns of loop antennas with varying diameters. ($\lambda = 10$ m is the wavelength in free space at 30 MHz.).

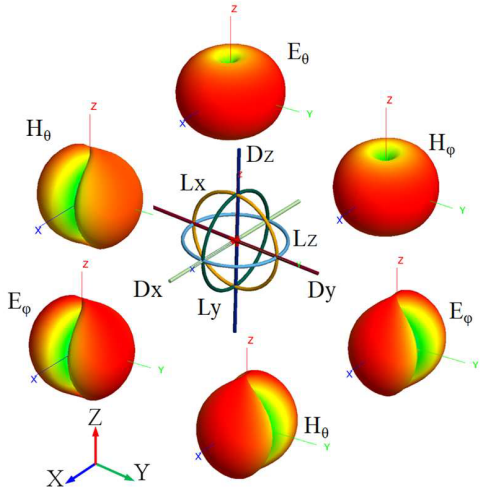

FIGURE 4. Simulated three-dimensional radiation patterns of the orthogonal dipole triad (Dx, Dy, Dz) and loop triad (Lx, Ly, Lz). (at 10 MHz).

each dipole exhibits a pronounced angle-dependent phase variation caused by the geometric factor.

As θ varies, the phase of each dipole output drifts continuously, and $\pm 180^\circ$ discontinuities appear when the geometric delay crosses integer multiples of π. This effect is especially evident for dipoles whose displacement has a larger projection along the incident wavevector. Consequently, the port phases of the non-CPC configuration no longer exhibit the stable, projection-only behavior observed in the CPC configuration; instead, they behave similarly to a small array with baseline-induced phase modulation. The simulated traces in Fig. 1(b) clearly reflect this behavior, demonstrating that spatial offsets introduce direction-dependent phase distortion even though the magnitude responses remain consistent with the expected dipole-field interaction.

These results confirm that non-CPC dipole arrangements fail to maintain a unified phase reference, thereby violating the phase-coherence requirement of a co-located electric-field vector sensor.

The simulations above evaluate only the electric-field responses of the dipole triad. However, the electric-field components alone are insufficient for fully characterizing an arbitrary HF wave [11]. A complete EMVA also requires complementary magnetic-field measurements, provided by three orthogonal loops. The loop responses supply the missing H-field information and complete the six-component EM field vector, enabling unambiguous polarization reconstruction, improved modal discrimination, and enhanced HF direction-of-arrival performance. Thus, the CPC dipole triad validated above forms the electric-field subsystem of the EMVA, while the loop triad extends the sensor to full vector capability. The evolution of the proposed EMVA is depicted in Fig. 2.

2.2. Dimension Optimization

As established in the preceding analysis, an electromagnetic vector antenna (EMVA) requires three mutually orthogonal dipoles to sense the electric-field components and three orthogonal loops to sense the magnetic-field components, forming a complete six-component vector sensor. For such a sensor to operate coherently, all six sensing elements must be arranged around a common phase center so that they sample the incident wave at the same spatial point without introducing baseline-dependent geometric phase errors. This requirement directly constrains the physical layout and, consequently, the achievable antenna dimensions.

Antenna size at HF is strongly constrained by the long wavelengths. Oversized elements introduce significant mechanical burden and complicate deployment, whereas excessively compact designs reduce effective height or loop area, degrading sensitivity [24]. To quantify these constraints, FEKO simulations of loop elements (Fig. 3) were performed. The results show that when the loop diameter increased to about 0.1λ ($\lambda =$

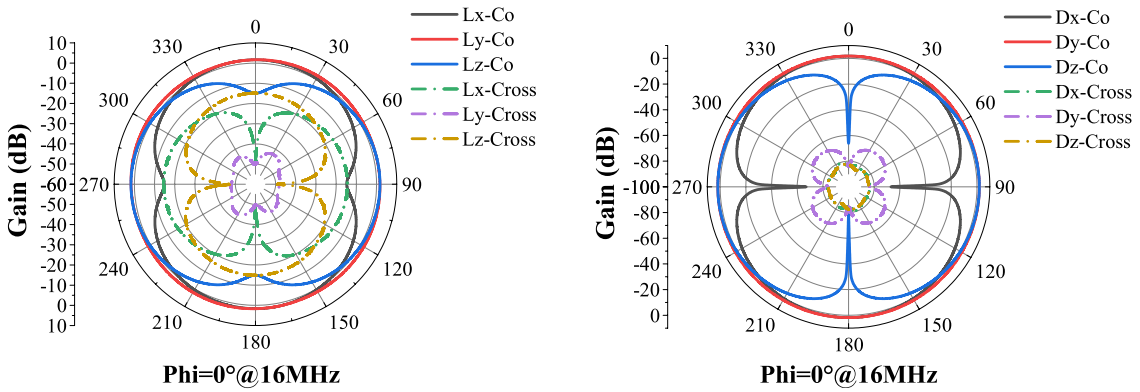

FIGURE 5. Two-dimensional co- and cross-polar radiation patterns of the dipole and loop triads at 16 MHz for $\phi = 0°$.

10 m is the wavelength in free space at 30 MHz), the induced circumferential current no longer maintains a uniform phase around the loop. Instead, portions of the loop carry opposing or phase-reversed currents, causing the nominal magnetic-dipole pattern to tilt, split, or deform above approximately 20 MHz. These observations highlight the need for a carefully selected loop size: restricting the loop diameter to 0.8 m (0.08λ at 30 MHz) effectively suppresses reverse-current effects and preserves a stable, dipole-like H-field response while maintaining structural compactness compatible with CPC implementation.

In contrast, linear dipoles tolerate larger electrical dimensions because the current distribution along a straight wire remains predominantly sinusoidal, and the broadside radiation pattern remains stable even as the length approaches 0.6λ. FEKO simulations confirm that dipoles up to 6 m in length exhibit minimal pattern distortion. Nevertheless, to maintain a compact CPC geometry and avoid excessive mechanical span, a dipole length of 2.2 m is adopted in the final design, providing a balanced compromise among effective height, structural rigidity and co-location with the loop triad.

With the dipole triad providing phase-coherent electric-field sensing at a common spatial origin and the loop triad supplying the complementary magnetic-field components, the resulting structure forms a fully co-located EMVA. This integrated optimization of dimensions and geometry ensures not only compactness but also stable vector-response behavior across the HF band, thereby providing the structural symmetry required for polarization-coherent and direction-sensitive HF measurements.

2.3. Radiation Pattern Analysis

The radiation characteristics of the dipole and loop elements were analyzed to confirm that the proposed EMVA maintains orthogonal vector-response behavior across the HF band and satisfies the CPC requirements established in Section 2. Since all six sensing elements operate as electrically small antennas over much of the 3–30 MHz range, pattern stability and inter-element isolation are essential for accurate vector-field reconstruction.

As illustrated in Fig. 4, the three orthogonal dipoles exhibit the expected figure-eight electric-dipole patterns, with nulls aligned along their respective axes, ensuring independent projections of the incident electric field. These patterns remain largely invariant across frequency, owing to the predominantly sinusoidal current distribution along the linear wires. The loop triad displays complementary magnetic-dipole behavior, with symmetric donut-shaped patterns and nulls along each loop normal. The optimized loop diameter (0.8 m) suppresses circumferential current reversal, thereby preventing pattern tilt or multi-lobe distortion and ensuring mutually independent H-field sensing.

To further validate these behaviors, Fig. 5 presents two-dimensional co- and cross-polar radiation patterns of the dipole and loop elements at 16 MHz for $\varphi = 0°$. The loop elements (Lx, Ly, Lz) maintain well-formed magnetic-dipole patterns, with cross-polar levels more than 20 dB below their co-polar responses across all elevation angles. Similarly, the dipole elements (Dx, Dy, Dz) retain clean figure-eight patterns with deep nulls along their axes and minimal cross-polarization. These results confirm that the chosen dipole and loop dimensions preserve pattern symmetry and orthogonality.

The CPC-based structural layout plays a central role in maintaining these characteristics. By co-locating the dipole and loop elements at a common spatial origin, the EMVA avoids direction-dependent phase discrepancies and angular skew that arise in non-CPC geometries. Together, the three-dimensional and two-dimensional pattern analyses verify that the EMVA provides well-conditioned and mutually orthogonal sensitivity to all six EM-field components (Ex, Ey, Ez, Hx, Hy, Hz), forming a robust foundation for multi-polarized HF sensing and high-accuracy angle-of-arrival estimation.

2.4. Structure Layout

Apart from antenna size, ground proximity significantly affects HF antennas. Traditional tri-axial arrangements suffer from inconsistent parameters and asymmetric radiation. The proposed ground-symmetric structure minimizes such effects. As shown in Fig. 6(a), geometric constraints fix the dipole orientation relative to the loops and ground. Because the dipole is orthogonal, so $\angle$ CAD equals 90°. Point E denotes the midpoint of CD. By applying basic geometric relations, $\angle\alpha$ is obtained as 54.736°, as shown in (1) and (2). The final structure (Figs. 6(b) and (c))

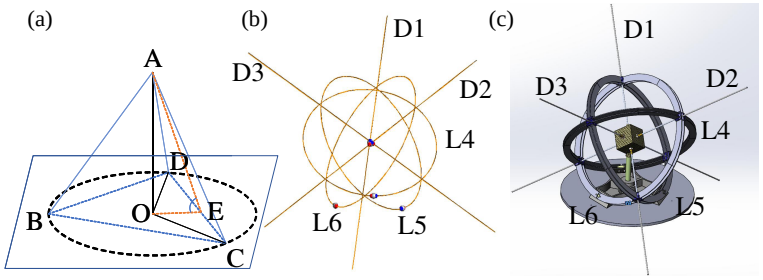

FIGURE 6. (a) Schematic diagram of antenna to ground relationship, (b) Antenna simulation model, and (c) Antenna structure design diagram.

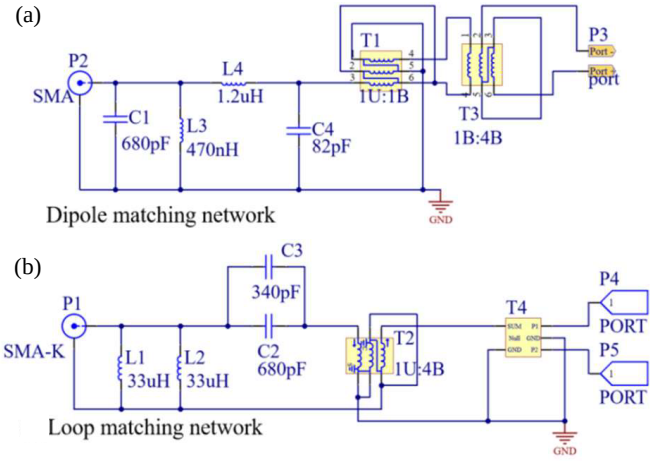

FIGURE 7. Schematic diagram of (a) dipole matching network and (b) loop matching network.

integrates three 2.2 m dipoles and three 0.8 m loops, achieving mechanical and electromagnetic symmetry.

$$\angle CAD = 90^\circ, \quad \angle COD = 120^\circ, \quad AC = AD \tag{1}$$

$$\angle AEO = \angle\alpha = \arcsin\left(\sqrt{2}/\sqrt{3}\right) \approx 54.736^\circ \tag{2}$$

The dipole antennas are positioned at the center of their corresponding loop antennas, aligned with the loop's axial direction. This geometric arrangement ensures that the angles between the dipoles and the ground are fully determined once the loop antenna's orientation is established. The resulting antenna model, illustrated in Fig. 6(b), comprises three orthogonal 2.2-meter dipoles and three orthogonal 0.8-meter loops, designed to sense the E-field and H-field, respectively.

In summary, the proposed multi-polarized antenna features a compact, ground-symmetrical structure that mitigates ground reflection effects, ensuring consistent radiation patterns for both dipoles and loops. This design is particularly suited for HF applications, where ground effects are significant.

3. PROTOTYPE IMPLEMENTATION AND TESTING

The proposed EMVA incorporates six sensing elements — three orthogonal dipoles and three orthogonal loops — each requiring an independent feed path in order to preserve vector orthogonality and maintain a common phase center (CPC). To achieve this, separate feeding and impedance-matching networks were implemented for the dipole triad and the loop triad.

3.1. Six-Port Feeding Architecture and Matching Network Design

The three dipole elements share a compact, PCB-based feed board positioned in a non-metal cube box at the geometric center of the EMVA. Each dipole is individually center-fed through a coaxial line and a balanced feed trace on the PCB. Ferrite current chokes are integrated at each feed point to suppress common-mode currents along the coaxial shields, ensuring that all three dipoles retain their intrinsic figure-eight response and maintain CPC phase consistency. Although the dipoles are physically mounted on the same board, their feed paths remain isolated to minimize inter-element coupling.

In contrast, the three-loop elements employ independent matching modules, each mounted close to the corresponding loop. Electrically small loop antennas are highly sensitive to feedline imbalance, and distributing the matching networks reduces parasitic coupling and prevents the feedlines from perturbing the magnetic-dipole patterns. Each loop is therefore fed through a dedicated transformer balun and a localized impedance-matching circuit.

In Fig. 7, ports P1 and P2 represent the 50-Ω excitation ports used for simulation and VNA measurements, emulating the input impedance of the receiver. Ports P3 and P4(P5) correspond to the antenna connection points, where the matched impedance is presented to the sensing elements.

Both the dipole and loop elements are electrically small across most of the 3–30 MHz HF range. Their input impedance can be expressed as:

$$Z_{in} \approx R_{rad} + R_{loss} + jX_{in} \tag{3}$$

where the radiation resistance R_{rad} is only a few ohms, while the reactive term X_{in} is large and varies rapidly with frequency. This combination makes direct 50 Ω matching extremely difficult, and a multi-stage compensation strategy is required to control the impedance trajectory across the HF band.

From the antenna side, the first component in both the dipole and loop paths are transformer-type balun (T1–T4 in Fig. 7). These transformers serve several purposes:

1. They perform impedance scaling according to $Z' = n^2 Z_{ant}$, effectively magnifying the small radiation resistance of the electrically small elements to a more manageable level;

TABLE 1. Comparison of representative HF vector-sensing/DOA antennas.

References	Antenna Type	Size/Aperture	Ports	Working Band	Isolation	Notes
[9]	Dipole/Loop Quads	Spatial spread	4–5	—	—	Large aperture, non-CPC
[12]	Two-port Crossed-loop and monopole	0.033λ height; 0.0467$\lambda \times$ 0.0467λ footprint	7	3–30 MHz	—	HF direction finding
[16]	Two-port Loop VA	Loop $\varnothing$0.033λ	2	HF	—	2-port vector sensing
[17]	Giselle	Loop $\varnothing$0.06λ; footprint $\sim$ 0.067λ	3-loops	3–30 MHz	—	Polarization-diverse HF RX
[20]	High isolation EMVS	Loop $\varnothing$0.05λ Dipole 0.1λ	6	3–30 MHz	$>$ 25 dB	EM signals distinguish
[23]	SuperCART	$\sim$ 0.09λ height; 0.04$\lambda \times$ 0.04λ footprint	6	HF	Low	CPC, early EMVS
Proposed EMVA (This Work)	Cross-loop and cross dipole	Dipole 0.0733λ; Loop $\varnothing$0.0267λ	6	3–30 MHz	$>$ 30 dB	Compact CPC, broadband, DoA

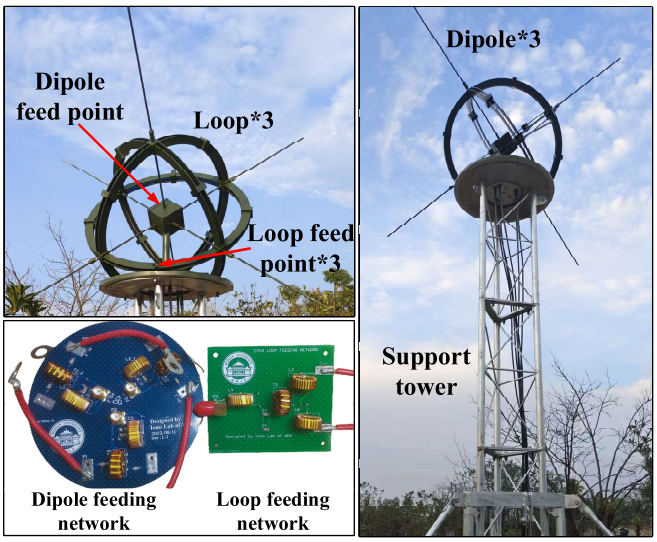

FIGURE 8. The photograph of the prototype of the proposed multi-polarized antenna.

2. They provide balanced-unbalanced conversion and help suppress common-mode currents on the feedlines, which is crucial for preserving the CPC and preventing pattern distortion;

3. They offer isolation between the antenna and subsequent LC matching stages.

By placing the balun directly at the antenna terminals (P3/P4), the subsequent LC network operates on a transformed impedance that is more resistive and less steep in frequency, which greatly facilitates broadband tuning.

As shown in Fig. 7, following the balun, each path includes a cascaded LC network that provides both coarse and fine reactive compensation. In the loop network, the series and shunt combinations of inductors and capacitors (e.g., L1-L2-C2-C3) first reduce the dominant loop reactance and flatten the impedance slope, effectively lowering the Q-factor and broadening the usable bandwidth. In the dipole network, the corresponding LC sections compensate the capacitive reactance of the electrically small dipoles and shape the impedance trajectory so that it gradually approaches the 50-Ω region on the Smith chart.

Additional shunt branches (such as the C-L tank connected after the balun) act as stabilizing networks: rather than enforcing a sharp resonance, they locally compress the impedance locus and improve high-frequency smoothness. The final LC adjustments in each path provide small rotations and translations of the impedance locus so that, over 3–30 MHz, the transformed impedance seen at ports P1/P2 remains close to 50 Ω with acceptable reflection level.

3.2. Prototype Assembly and Testing

A photograph of the fabricated EMVA prototype is shown in Fig. 8. The antenna consists of a mechanically orthogonal triad of 2.2-m dipoles and a co-located triad of 0.8-m loops, all referenced to the same geometric center to preserve the CPC configuration. The dipole feed board is mounted at the antenna core, while each loop incorporates an independent matching module placed near its terminals. All six feedlines are routed symmetrically toward the base to avoid structural asymmetry.

Figure 9 summarizes the measured RF characteristics. The insertion loss of the dipole and loop matching networks [Fig. 9(a)] follows the expected transformer-dominated behavior, improving from approximately -16 to -6 dB (dipoles) and -18 to -10 dB (loops) over 3–30 MHz. The VSWR results in Fig. 9(b) indicate broadband matching, with the three dipole ports maintaining VSWR $<$ 2 across most of the HF band and the loop ports achieving VSWR between 1.2 and 1.8, consistent with electrically small loop behavior.

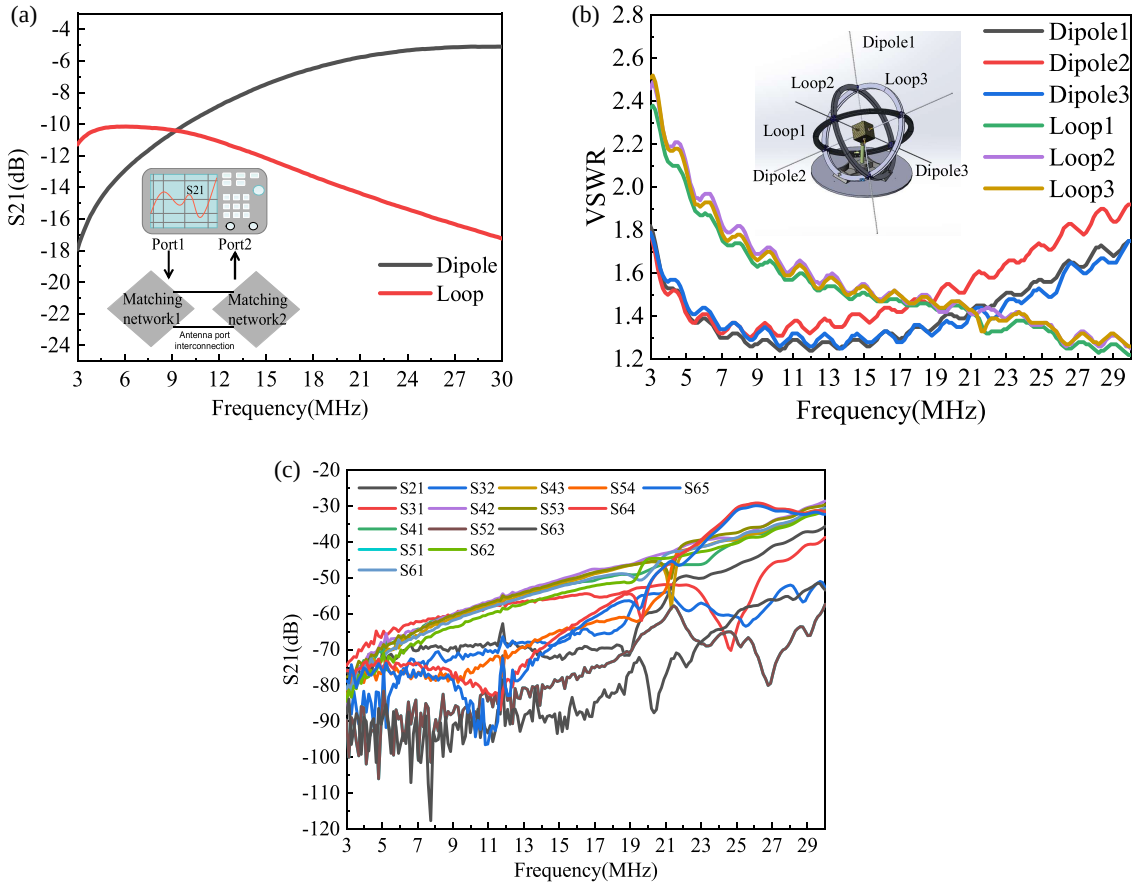

FIGURE 9. Measured results. (a) Insertion loss of the matching network, (b)VSWR, and (c) S21 between each port.

The measured port isolation [Fig. 9(c)] exceeds 20 dB for all dipole-dipole, loop-loop, and dipole-loop combinations across the operating band. This high isolation is attributed to the CPC geometry, symmetric structure, independent matching modules, and common-mode suppression provided by the transformer baluns.

Collectively, these measurements confirm that the prototype EMVA achieves stable broadband matching and strong inter-port decoupling, forming a robust basis for multi-polarized HF vector sensing and subsequent direction-finding experiments.

3.3. Comparison of Representative HF Vector-Sensing/DOA Antennas

Table 1 provides a brief comparison between the proposed EMVA and representative HF vector-sensing and DOA-capable antennas. Earlier structures, such as dipole/loop quads, rely on spatially separated elements, resulting in non-CPC geometries, large physical apertures, and limited isolation. Two-port loop-based vector antennas offer partial magnetic-field sensing but lack full six-component capability. Other polarization-diverse HF receivers (e.g., Giselle) maintain stable loop patterns and yet do not realize complete vector-field measurements.

In contrast, the proposed EMVA achieves a compact CPC configuration with electrically small dimensions (dipole 0.0733λ, loop 0.0267λ at 10 MHz), full six-port vector sensing, broadband 3–30 MHz operation, and isolation exceeding 30 dB. This combination of compact size, CPC integrity, and high isolation distinguishes the antenna from prior HF vector-sensing solutions and supports accurate polarization-diverse HF direction finding.

4. EXPERIMENTAL VALIDATION

To assess the direction-finding performance of the proposed EMVA, an 11-MHz continuous-wave (CW) ionospheric-sounding experiment was conducted on 10 October 2024. The transmitter at Wuhan University and the receiver located 70 km away enabled simultaneous reception of both ordinary (O-mode) and extraordinary (X-mode) returns, providing a practical test scenario for multi-polarized HF sensing.

Figure 10 shows the estimated arrival angles together with reference angles derived from the IRI-2016 model. Because IRI assumes a horizontally stratified ionosphere, the theoretical angles serve only as smooth background references rather than true ground-truth DOA values.

For the O-mode signals, the EMVA achieved RMS errors of 10.02° (azimuth) and 8.42° (elevation). For the X-mode, the corresponding RMS errors were 14.77° and 26.09°.

These results demonstrate accurate six-component field reconstruction and reliable O/X-mode discrimination under real propagation conditions.

The remaining discrepancies stem from well-known factors: (i) ionospheric gradients and layer tilts not represented in IRI;

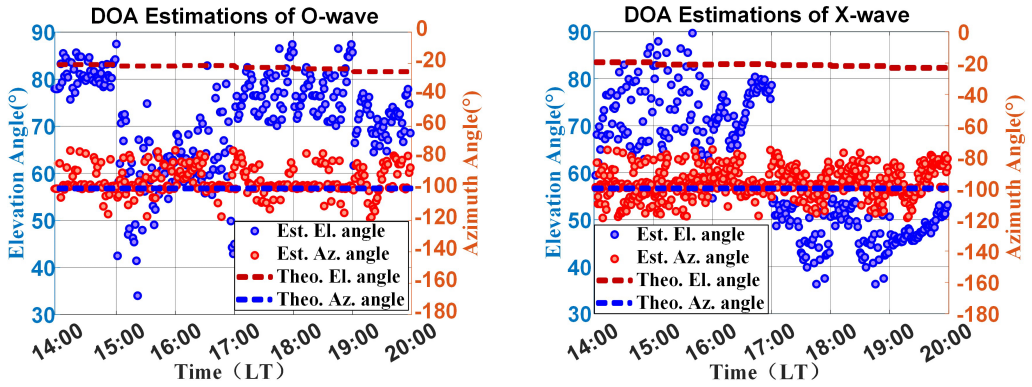

FIGURE 10. The measured results of DOA with the proposed multi-polarized antenna.

(ii) magneto-ionic effects such as O/X-mode splitting, polarization evolution and weak multipath; and (iii) residual system imperfections, including amplitude–phase imbalance and environmental scattering. The larger elevation error in the X-mode reflects its stronger sensitivity to horizontal irregularities and steeper refractive-index gradients near the reflection region, rather than limitations of the antenna.

Overall, the field experiment verifies that the compact CPC EMVA provides stable multi-polarized reception and accurate HF DOA estimation, supporting its use in short-baseline ionospheric sensing and polarization-diverse HF monitoring.

5. CONCLUSION

This work has presented a compact, fully co-located electromagnetic vector antenna (EMVA) capable of broadband six-component field sensing across the 3–30 MHz HF band. By combining orthogonal dipoles and loops within a strict common-phase-center geometry and employing transformer-assisted multi-stage matching networks, the proposed design achieves stable impedance characteristics and port isolation exceeding 30 dB while maintaining an electrically small footprint. Full-wave simulations and prototype measurements confirm that the antenna preserves the intended vector-response orthogonality and provides well-conditioned inputs for polarization-diverse processing.

Field validation using an 11-MHz ionospheric-sounding link demonstrated accurate O-/X-mode angle-of-arrival estimation, with RMS errors of $10.02°/8.42°$ for the O-mode and $14.77°/26.09°$ for the X-mode. The results verify the EMVA's capability to perform reliable HF direction finding under real ionospheric conditions and highlight its suitability for compact HF sensing platforms, polarization-coherent receivers, and short-baseline ionospheric monitoring. Future work will focus on refined calibration procedures and extended-array configurations to further enhance DOA accuracy and polarization-resolution performance.

ACKNOWLEDGEMENT

This work was supported by the National Natural Science Foundation of China under Grants 42304170, 41574146, U23B2016, and 42104150, the National Key Research and Development Program of China under Grant 2023YFA1009100 and 2023YFB3905100.

REFERENCES

[1] Nehorai, A. and E. Paldi, "Vector-sensor array processing for electromagnetic source localization," *IEEE Transactions on Signal Processing*, Vol. 42, No. 2, 376–398, Feb. 1994.

[2] Piao, D. and Y. Wang, "Tripolarized mimo antenna using a compact single-layer microstrip patch," *IEEE Transactions on Antennas and Propagation*, Vol. 67, No. 3, 1937–1940, Mar. 2019.

[3] Giuli, D., "Polarization diversity in radars," *Proceedings of the IEEE*, Vol. 74, No. 2, 245–269, Feb. 1986.

[4] Andrews, M. R., P. P. Mitra, and R. DeCarvalho, "Tripling the capacity of wireless communications using electromagnetic polarization," *Nature*, Vol. 409, No. 6818, 316–318, 2001.

[5] Stutzman, W. L., *Polarization in Electromagnetic Systems*, Artech House, 2018.

[6] Chacko, B. P., G. Augustin, and T. A. Denidni, "Uniplanar slot antenna for ultrawideband polarization-diversity applications," *IEEE Antennas and Wireless Propagation Letters*, Vol. 12, 88–91, 2013.

[7] Randazzo, A., M. A. Abou-Khousa, M. Pastorino, and R. Zoughi, "Direction of arrival estimation based on support vector regression: Experimental validation and comparison with music," *IEEE Antennas and Wireless Propagation Letters*, Vol. 6, 379–382, 2007.

[8] Lu, B., B. Wen, Y. Tian, and R. Wang, "Analysis and calibration of crossed-loop antenna for vessel doa estimation in hf radar," *IEEE Antennas and Wireless Propagation Letters*, Vol. 17, No. 1, 42–45, Jan. 2018.

[9] Yuan, X., "Spatially spread dipole/loop quads/quints: For direction finding and polarization estimation," *IEEE Antennas and Wireless Propagation Letters*, Vol. 12, 1081–1084, 2013.

[10] Sarkis, R. and C. Craeye, "Fast full-wave analysis of wideband circular antenna arrays devoted to accurate direction-finding and polarimetry," in *2012 International Conference on Electromagnetics in Advanced Applications*, 784–787, Cape Town, South Africa, 2012.

[11] Tang, W., W. Qu, L. You, T. Li, J. Xin, and S. Yang, "Estimation and separation of ionospheric narrow-band unknown o and x waves," *IEEE Transactions on Antennas and Propagation*, Vol. 71, No. 1, 892–901, Jan. 2023.

[12] Knapp, M., R. Volz, F. D. Lind, F. C. Robey, A. Fenn, K. Johnson, M. Silver, A. Morris, and S. Klein, "HF vector sensor for radio astronomy: Ground testing results," in *AIAA SPACE 2016*, 5498, 2016.

[13] Harris, T. J., M. A. Cervera, L. H. Pederick, and A. D. Quinn, "Separation of o/x polarization modes on oblique ionospheric soundings," *Radio Science*, Vol. 52, No. 12, 1522–1533, 2017.

[14] Yuan, X., K. T. Wong, and K. Agrawal, "Polarization estimation with a dipole-dipole pair, a dipole-loop pair, or a loop-loop pair of various orientations," *IEEE Transactions on Antennas and Propagation*, Vol. 60, No. 5, 2442–2452, May 2012.

[15] Wong, K. T., "Direction finding/polarization estimation-dipole and/or loop triad (s)," *IEEE Transactions on Aerospace and Electronic Systems*, Vol. 37, No. 2, 679–684, Apr. 2001.

[16] Meloling, J. H., J. W. Rockway, M. P. Daly, A. R. Monges, J. C. Allen, W. R. Nielsen, P. M. McGinnis, R. B. Thompson, and N. A. Mozaffar, "A vector-sensing antenna system: A high-frequency, vector-sensing array based on the two-port loop antenna element," *IEEE Antennas and Propagation Magazine*, Vol. 58, No. 6, 57–63, Dec. 2016.

[17] Martinsen, W., "Giselle: A mutually orthogonal triple twin-loop ground-symmetrical broadband receiving antenna for the HF band," Tech. Rep., Defence Science and Technology Organisation, Department of Defence, Australian Government, 2009.

[18] Wang, X., Y. Guo, F. Wen, J. He, and T.-K. Truong, "EMVS-MIMO radar with sparse Rx geometry: Tensor modeling and 2-D direction finding," *IEEE Transactions on Aerospace and Electronic Systems*, Vol. 59, No. 6, 8062–8075, Dec. 2023.

[19] Wen, F., Z. Zhang, H. Sun, G. Gui, H. Sari, and F. Adachi, "2D-DOA estimation auxiliary localization of anonymous UAV using EMVS-MIMO radar," *IEEE Internet of Things Journal*, Vol. 11, No. 9, 16 255–16 266, May 2024.

[20] Tong, K., Y. Liu, Y. Ma, and D. Li, "Design of high isolation electromagnetic vector antenna," in *2024 14th International Symposium on Antennas, Propagation and EM Theory (ISAPE)*, 1–4, Hefei, China, 23-26 2024.

[21] Chen, H., J. Fang, W. Wang, W. Liu, Y. Tian, Q. Wang, and G. Wang, "Near-field target localization for emvs-mimo radar with arbitrary configuration," *IEEE Transactions on Aerospace and Electronic Systems*, Vol. 60, No. 4, 5406–5417, Aug. 2024.

[22] Kononov, E., M. Knapp, A. Morris, F. Lind, F. Robey, and K. Cahoy, "Sensitivity of an electromagnetic vector sensor," in *2024 IEEE Aerospace Conference*, 1–8, Big Sky, MT, USA, 2024.

[23] Farina, D. J., "Superresolution compact array radiolocation technology (supercart) project," *Flam and Russell Tech. Rep.*, Vol. 185, 1990.

[24] Sarabandi, K. and M. Rao, "Bandwidth and snr of small receiving antennas: To match or not to match," *IEEE Transactions on Antennas and Propagation*, Vol. 71, No. 1, 99–104, Jan. 2023.